Materials Advances

ROYAL SOCIETY OF CHEMISTRY

PAPER

View Article Online
View Journal | View Issue

Cite this: *Mater. Adv.*, 2022, 3, 9111

Tuning of hole carrier density in p-type α-$SnWO_4$ by exploiting oxygen defects†

Makoto Minohara, *[a] Yuka Dobashi,[ab] Naoto Kikuchi,[a] Akane Samizo,[b] Takashi Honda,[cd] Xinyi He,[e] Takayoshi Katase,[e] Toshio Kamiya,[e] Keishi Nishio[b] and Yoshihiro Aiura[a]

Received 11th July 2022,
Accepted 7th November 2022

DOI: 10.1039/d2ma00815g

rsc.li/materials-advances

The development of p-type oxide semiconductors has shown promise in overcoming limitations restricting the practical usage of oxide semiconductors and the realization of innovative functional devices. Through numerous studies based on both experimental and theoretical approaches, several state-of-the-art p-type oxide semiconductors have been discovered. However, one of the challenges concerning these p-type oxide semiconductors is on tuning the hole carrier density. In this study, precise tuning of the hole carrier density in α-$SnWO_4$ based on thermodynamic condition control was demonstrated. A detailed investigation of the crystal structure *via* X-ray diffraction, extended X-ray absorption fine structures, and density functional theory calculations revealed the role of oxygen defects, such as oxygen vacancies and interstitials, in tuning the hole carrier density. This study shows the importance of fine-tuning of oxygen defects based on thermodynamic condition control for the emergence and improvement of p-type semiconducting properties in Sn^{2+}-based oxides.

Introduction

Wide-bandgap oxide semiconductors, such as ZnO, In_2O_3, and Ga_2O_3, are promising materials for the development of innovative (opto-)electronic devices based on their transparency and high breakdown voltage.[1] However, because of the characteristic electronic configurations of their valence bands, these wide-bandgap oxide semiconductors are mostly of the n-carrier type, and consequently, the potential of these semiconductors for practical application is presently limited. One of the strategies to overcome this limitation is the development of p-type oxide semiconductors *via* the modulation of the valence band.[2–6]

Based on an analogy with the amorphous n-type oxide semiconductors $InGaZnO_4$ and Sn-doped In_2O_3, oxide semiconductors with ns^2 ($n \geq 5$) orbitals in their valence band maxima (VBM) are expected to have small effective masses for holes because of the dispersive band edges and high tolerance features for structural disordering arising from their spatially spreading orbitals.[7,8] Indeed, SnO films with VBMs comprising the Sn $5s^2$ orbital exhibit negligible differences in hole mobility between epitaxially grown and polycrystalline structures. However, the growth conditions required to obtain the highest mobility of 18–20 $cm^2\ V^{-1}\ s^{-1}$ for SnO are considerably limited because of its chemical instability.[3,9–11]

Recently, several p-type oxide semiconductors with ns^2 orbitals have been developed based on predictions through theoretical approaches.[12–17] These state-of-the-art p-type oxide semiconductors can be categorized into two groups: one is for Sn^{2+}-based oxide semiconductors, such as pyrochlore-type $Sn_2TM_2O_7$ (TM = Nb or Ta)[13] and layered-structure $SnNb_2O_6$ and α-$SnWO_4$;[14,15] and the other is for Bi^{3+}-based oxide semiconductors, such as perovskite-type $BaBiO_3$,[16] double-perovskite-type Ba_2BiTMO_6,[12,16] and pyrochlore-type $Bi_2Sn_2O_7$.[17] Of the two, Sn^{2+}-based oxide semiconductors are less chemically stable than Bi^{3+}-based ones because of their metastable Sn^{2+} states. However, this disadvantage is expected to be overcome *via* the selection of an appropriate crystal structure based on phase stability.[18] On the other hand, the hole carrier densities of Sn^{2+}-based oxide semiconductors (10^{17}–10^{18} cm^{-3}) are several orders of magnitude greater than those of Bi^{3+}-based ones (10^{13}–10^{14} cm^{-3}).[12–17] Such

[a] *Research Institute for Advanced Electronics and Photonics, National Institute of Advanced Industrial Science and Technology (AIST), Tsukuba, Ibaraki, 305-8568, Japan. E-mail: m-minohara@aist.go.jp; Tel: +81-29-862-6475*
[b] *Department of Materials Science and Technology, Tokyo University of Science, Katsushika, Tokyo, 125-8585, Japan*
[c] *Materials & Life Science Division, J-PARC Centre, Tokai, Ibaraki, 319-1195, Japan*
[d] *Institute of Materials Structure Science, High Energy Accelerator Research Organization (KEK), Tsukuba, Ibaraki, 305-0801, Japan*
[e] *Laboratory for Materials and Structures, Institute of Innovative Research, Tokyo Institute of Technology, 4259 Nagatsuta, Midori, Yokohama, 226-8503, Japan*

† Electronic supplementary information (ESI) available: Thermopower *versus* temperature difference, optical band gap, lattice constants of *a*, *b*, and *c*-axes, and Sn/W ratio of α-$SnWO_4$ samples (S1–S4), plots of intensity in EXAFS spectra (S5), and calculated bond lengths of candidate structures (S6). See DOI: https://doi.org/10.1039/d2ma00815g

characteristics of Sn^{2+}-based oxide semiconductors in terms of carrier density are useful for designing electronic devices with high conductivities.

In this regard, precise tuning of the carrier densities of Sn^{2+}-based p-type oxide semiconductors is highly necessary. However, intentional control over the hole carrier density remains a challenging undertaking.[17,19–22] Especially, Sn^{2+}-based oxides in the thin-film form still show the insulating properties.[19–22] This is likely because oxygen vacancies form spontaneously to compensate for the positive charge.[19,20,23] For example, in α-$SnWO_4$, the net hole carrier density is determined by a balance between the following defect formations, as shown by this Kröger–Vink notation:

$$Sn(II)^{\times}_{Sn(II)} + O_2 \rightleftharpoons V''_{Sn(II)} + Sn(IV)''_W + 2O^{\times}_O + 4h^{\bullet} \quad (1)$$

$$2O^{\times}_O \rightleftharpoons 2V^{\bullet\bullet}_O + O_2 \uparrow (gas) + 4e' \quad (2)$$

where $Sn(II)^{\times}_{Sn(II)}$ and $O^{\times}_O$ are Sn^{2+} at the original Sn site and O^{2-} at the original O site, respectively; and $V^{\bullet\bullet}_O$ is the oxygen vacancy. Here, we assume the formation of an additional sublattice composed of $Sn(IV)''_W$ and $O^{\times}_O$, as previously reported.[24] $Sn(IV)''_W$ is the Sn^{4+} substitutional defect at the W^{6+} site, and $V''_{Sn(II)}$ corresponds not to the tin vacancy due to evaporation from the material but to the resultant void due to the formation of $Sn(IV)''_W$.[15,24] Meanwhile, $h^{\bullet}$ and e' denote the holes and electrons, respectively. As a result, the hole carrier generation efficiencies of Sn^{2+}-based oxide semiconductors from Sn^{4+} substitutional defects are tremendously low, as low as 0.005–1.4%; the efficiencies of layered-structure Sn^{2+}-based oxide semiconductors are much greater than that of pyrochlore-type ones.[13,14,24] This is due to electrostatic interaction between electron densities at Sn^{2+} ions and surrounded O^{2-} ions.[24] Therefore, the layered-structure Sn^{2+}-based oxide semiconductors should be promising materials showing high hole carrier densities.

Here, it can be expected that the net hole carrier density would increase at oxidizing conditions because the numbers of holes and electrons are increased and decreased, respectively, based on eqn (1) and (2), respectively. On the other hand, the optimum conditions may be limited by the metastable Sn^{2+} valence state and the valence-fluctuating nature of transition metal ions. Prior to investigating the conditions for emerging the p-type conductivity of Sn^{2+}-based oxide films, it is essential that precise information on the manipulation of oxygen defects in those bulk forms with the p-type conductivities.[14,15] In this study, we demonstrate that precise control over the O_2 gas concentration during the annealing process is effective for tuning the hole carrier density of α-$SnWO_4$. The hole carrier density increased by two orders of magnitude and achieved a value close to 10^{19} cm^{-3}, which is comparable with the highest carrier density of SnO,[3] at an optimum O_2 gas concentration.

Experimental section

Synthesis

Samples of α-$SnWO_4$ were synthesized *via* a solid-state reaction. Here, SnO (Kojundo Chemical Laboratory; purity 99.5%) and WO_3 (Kojundo Chemical Laboratory; purity 99.9%) were mixed in an agate mortar with ethanol, after which the mixed powders were dried in air for 24 h and then calcined at 600 °C in a tube furnace under N_2 at a flow rate of 150 ml min^{-1}. At this point, the synthesis of α-$SnWO_4$ samples was completed. After synthesis, 2 wt% polyvinyl alcohol aqueous solution was added, and the mixture was stirred for 15 min, which was followed by sieving to obtain narrow sieve fractions of <212 μm. The obtained powder was pressed uniaxially at 270 MPa and then isostatically at 290 MPa to form tablets with a diameter of 12 mm and thickness of 1 mm. The samples were annealed at 650 °C in a tube furnace under an N_2/O_2 gas mixture at a total flow rate of 50 ml min^{-1}. The concentration of O_2 gas was controlled to be within the range 0–100 ppm *via* the ratio of the flow rates of the N_2 and O_2 gases.

Characterization

The chemical compositions of the samples were determined using a wavelength-dispersive X-ray fluorescence (XRF) spectrometer (Rigaku ZSX). Diffuse reflectance spectra were measured using a double-beam ultraviolet-visible spectrometer with an integrating sphere (Shimadzu UV-2550) and converted into absorption spectra using the Kubelka–Munk method. The carrier types of the α-$SnWO_4$ samples were determined based on the sign of the Hall and Seebeck coefficients (measured using the Resitest 8310 (Toyo Corp.) and ZEM-3 (ADVANCE RIKO Inc.) measurement systems, respectively).

The crystal structure and lattice parameters were analyzed *via* X-ray diffraction (XRD) using the Bragg–Brentano configuration with Cu Kα radiation (PANalytical, X'Pert Pro MPD) and synchrotron-based XRD (SR-XRD), which was performed at beamline BL-8B at the Photon Factory (PF), KEK. The energy of the incident synchrotron-based X-rays was 18 keV. The structural parameters were refined *via* Rietveld analysis using Z-Rietveld ver. 1.1.11,[25,26] and crystal structures were drawn using VESTA.[27] The local crystal structures were investigated using extended X-ray absorption fine structure (EXAFS) measurements at 40 K. Sn K- and W L_3-edge EXAFS measurements in the transmission mode were acquired at beamline AR-NW10A[28] of the KEK PF Advanced Ring and at BL-9A of the PF, respectively. The EXAFS spectra were Fourier transformed using the Hanning window function within a *k* range of 3–17 Å for both the Sn K- and W L_3-edges. The EXAFS spectra were processed using Athena.[29]

Density functional theory (DFT) calculation

DFT calculations for α-$SnWO_4$ were conducted using the projector augmented wave (PAW) method implemented in the Vienna *Ab initio* Simulation Package (VASP).[30,31] Sn [4d5s5p], W [5s5p5d6s], and O [2s2p] were included as valence states. The O vacancy and interstitial defect models ($SnWO_{3.75}$ and

$SnWO_{4.25}$) were built based on the removal or addition of one O atom from or to a fully relaxed α-$SnWO_4$ unit cell (four Sn atoms, four W atoms, and 16 O atoms). All variable-cell structure relaxations were performed using the generalized gradient approximation (GGA) Perdew–Burke–Ernzerhof revised for solids (PBEsol) functional[32] with a plane wave cut-off energy of 550 eV and a gamma-centered *k*-spacing of 0.1 $Å^{-1}$. The internal atomic coordinates were fully relaxed until the total energy difference was smaller than 10^{-6} eV and all the forces on the atoms became less than 0.01 eV $Å^{-1}$.

Results and discussion

XRD measurements were performed to investigate the effect of annealing on the crystal structures of the α-$SnWO_4$ samples. Fig. 1 shows the XRD 2θ–θ patterns for the α-$SnWO_4$ samples after annealing at O_2 gas concentrations of 0–100 ppm. The observed XRD patterns well describe the single-phase α-$SnWO_4$; the annealed samples are free from any side effects, such as the generation of impurity phases or disproportionation to Sn metal and Sn^{4+} compounds. When the O_2 gas concentration was 0.4%, the sample was completely decomposed into SnO_2 and WO_3.

Fig. 2 shows the carrier densities of α-$SnWO_4$ samples annealed at different O_2 gas concentrations after synthesis. The Seebeck coefficients were positive for all samples (Fig. S1, ESI†), indicating a p-carrier type (holes) conduction. From 0 to 30 ppm, the carrier density increased monotonically from 7×10^{16} cm^{-3} to 8×10^{18} cm^{-3}. The high carrier densities have been maintained one year after the initial characterization. When the O_2 gas concentration was ≥40 ppm, the carrier density decreased until it was maintained at a final value of 6×10^{17} cm^{-3}. While the carrier density changed as a function of the O_2 gas concentration, the optical band gap changed only negligibly (Fig. S2, ESI†).

The former trend can be explained by the suppression of $V_O^{\bullet\bullet}$ formation; however, the latter cannot be explained by the expected defect formation (eqn (1) and (2)). To clarify the mechanism of the carrier density changes, we investigated the crystal structure change. Plots of the unit-cell volume as a function of the O_2 gas concentration during annealing are shown in Fig. 3. Here, the unit-cell volume was estimated based

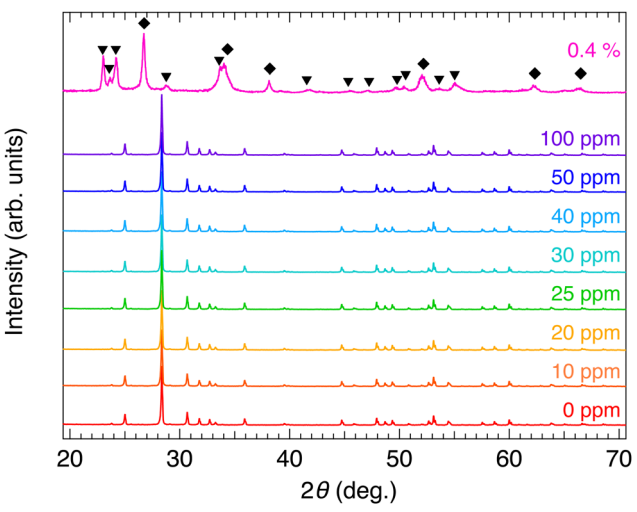

Fig. 1 2θ–θ X-ray diffraction patterns of α-$SnWO_4$ samples for different O_2 gas concentrations during annealing after synthesis. Triangles and diamonds in the XRD pattern of 0.4% sample correspond to the decomposed WO_3 and SnO_2, respectively.

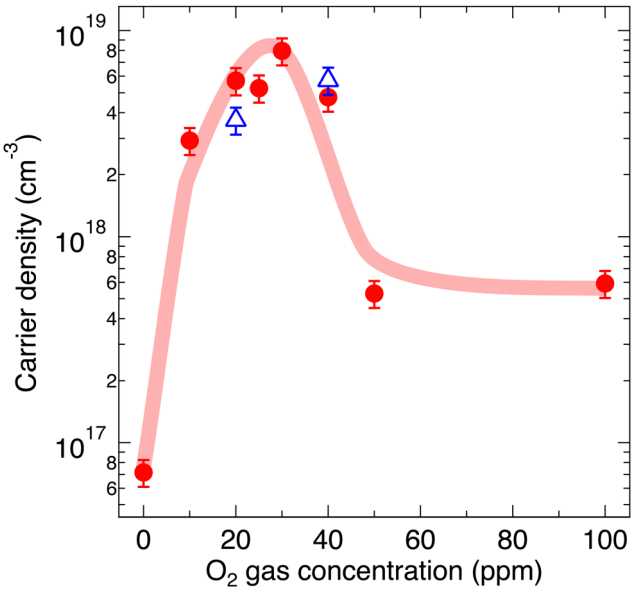

Fig. 2 Carrier densities at room temperature of α-$SnWO_4$ samples as function of O_2 gas concentration. The solid line is guide. Triangles correspond to the data measured one year after the initial measurements (circles).

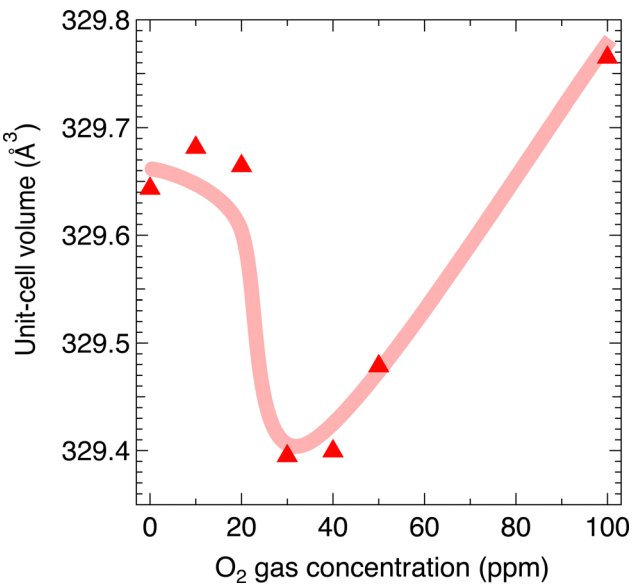

Fig. 3 Plots of unit-cell volume obtained through Rietveld analysis of 2θ–θ X-ray diffraction patterns of α-$SnWO_4$ samples as function of O_2 gas concentration. The solid line is guide.

on the lattice constants of a, b, and c axes obtained through Rietveld analyses of the XRD 2θ–θ patterns (Fig. S3, ESI†). As the O_2 gas concentration increased, the unit-cell volume decreased when the O_2 gas concentration was $\leq$30 ppm, whereas the unit-cell volume increased when the O_2 gas concentration was $\geq$40 ppm. This result suggests that the observed trend for the carrier density (Fig. 2) originates from the unit-cell volume and associated local structure changes (Fig. 3).

Based on a unit-cell volume of 326.46 Å^3 for the ideal α-$SnWO_4$ obtained *via* our DFT calculation, the decrease in unit-cell volume for the samples annealed at O_2 gas concentrations in the range 0–30 ppm is most likely explained by the suppression of $V_O^{\bullet\bullet}$ formation.[33] By contrast, the increase in unit-cell volume at above 40 ppm cannot be naturally explained by $V_O^{\bullet\bullet}$ regeneration at higher O_2 gas concentrations. Cation non-stoichiometry in complex oxides is well known to be a possible cause of lattice expansion;[34] however, a nearly stoichiometric Sn/W ratio was confirmed *via* XRF measurements for all samples (Fig. S4, ESI†). At this point, what remains to be analyzed is the possibility of interstitial oxygen defects (O_i).[35] α-$SnWO_4$ is composed of an alternating structure of WO_6 octahedra and Sn^{2+} layers, and thus it is inferred that repulsions between lone-pair electrons will create a rather large space in the crystal structure. Therefore, it is expected that O_i can be formed around the Sn^{2+} ions.

Our DFT calculations confirmed these inferences, namely, on the expansion of the unit-cell volume by $V_O^{\bullet\bullet}$ or O_i formation. The α-$SnWO_4$ contains oxygen ions of two types; four O^{2-} ions (O(1)), each connected to a nearest-neighbor WO_6 octahedron, and O^{2-} ion pairs (O(2)) supporting the Sn^{2+} layer (Fig. 4A). In the case of p-type α-$SnWO_4$, $V_O^{\bullet\bullet}$ is preferentially formed at the O(2) site.[15] The unit-cell volume of α-$SnWO_4$ with $V_O^{\bullet\bullet}$ at the O(2) site was calculated to be 330.65 Å^3 indicating the expansion of the unit-cell volume. On the other hand, to determine the effects of O_i formation, the unit-cell volumes were calculated for six models with different O_i site (Fig. 4A–F). The calculated values of unit-cell volume with respect to O_i formation are shown in Fig. 4G. These six models can be categorized into three groups based on the following criteria: O_i formation on the Sn^{2+} layer (A and B), O_i formation on the WO_6 octahedral layer (E and F), and O_i formation between the Sn^{2+} and WO_6 octahedral layers (C and D). Of these, cases A to D exhibited unit-cell volume expansion. Therefore, α-$SnWO_4$ annealed at higher oxygen concentrations (*e.g.*, 100 ppm) may have O_i around the Sn^{2+} ions.

To obtain further insight into the oxygen defects in the α-$SnWO_4$ samples, EXAFS measurements were performed. Fig. 5A and B show the representative Fourier-transform (FT) magnitudes of the EXAFS data for the Sn K- and W L_3-edges, respectively. These spectra exhibit two prominent features at 1.5–1.8 Å and 3.2–3.5 Å, caused by single scattering from the O and Sn/W atoms, respectively. Based on an assumption that the Debye–Waller factor of each atom does not change, the changes in intensity reflect the number of oxygen atoms. The intensity of the FT corresponding to the contributions of the nearest-neighbor (NN) Sn–O scattering peak was nearly unchanged from 0 ppm to 40 (or 50) ppm and clearly increased when the O_2 gas concentration was above 50 ppm (see also Fig. S5, ESI†). By contrast, the intensity of the W–O scattering peaks was maintained for all samples.

Quantitatively, the carrier density changes (from 7×10^{16} cm^{-3} to 8×10^{18} cm^{-3}) in the range 0 to 30 ppm correspond to a change in the concentration of $V_O^{\bullet\bullet}$ from

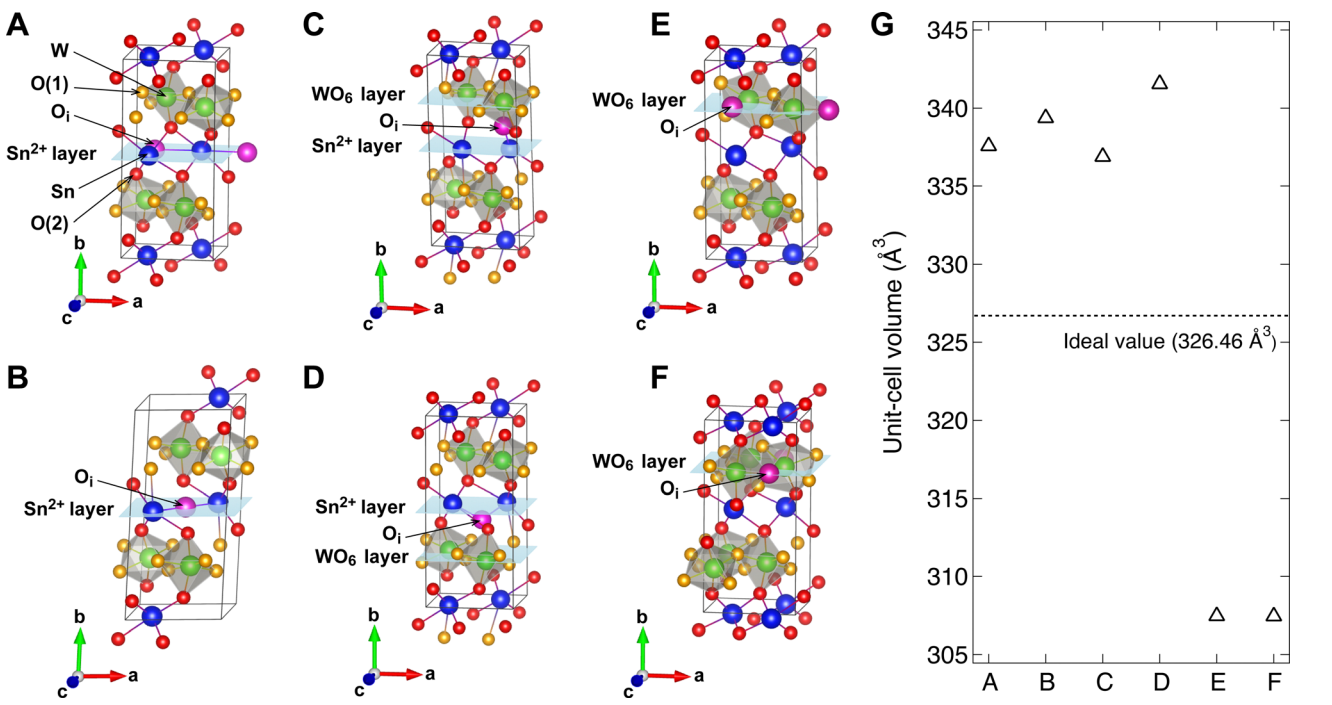

Fig. 4 (A–F) Candidate structures of interstitial oxygen in α-$SnWO_4$ samples for DFT calculations. (G) Calculated unit-cell volume of α-$SnWO_4$ with O_i formed at each position.

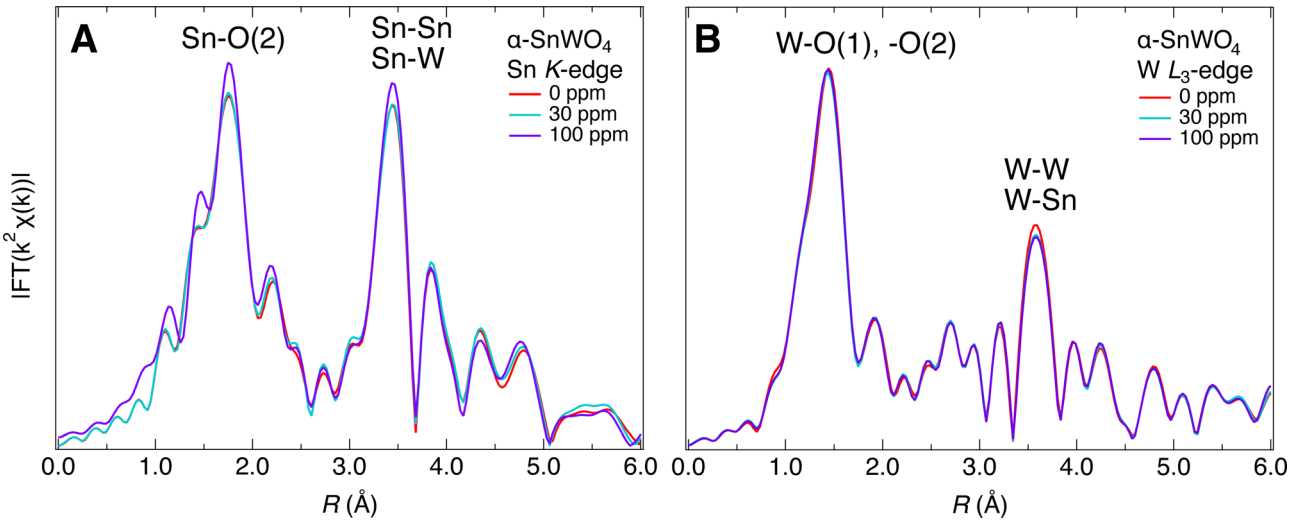

Fig. 5 k^2-Weighted Fourier-transformed (A) Sn K-edge and (B) W L_3-edge spectra of representative α-$SnWO_4$ samples. *R* is interatomic distance without correction obtained from photoelectron phase shift.

0.87 at% to 0.86 at% at a constant concentration of Sn''_W of 3.5 at%.[15] However, in actuality, the changes in the concentration of $V_O^{\bullet\bullet}$ should be less than the estimated values because the increment in the O_2 gas concentration will affect not only the amount of $V_O^{\bullet\bullet}$ but also that of Sn''_W, as mentioned in the introductory section. In this case, negligible changes in the intensities of the Sn–O and W–O scattering peaks would be reasonable. Here, it should be an important fingerprint for the O_i that a clear increment in the intensity was observed only for the Sn–O scattering peaks, which are composed of Sn–O(2) bonds, at higher O_2 gas concentrations. If the amount of oxygen at the O(2) site in α-$SnWO_4$ increases, a similar trend is expected for the intensities of the W–O scattering peaks because these peaks contain both W–O(1) and W–O(2) bonds. Therefore, it is possible that the prominent features at ∼1.8 Å in the FT magnitude of the EXAFS data for the Sn K-edge (Fig. 5A) reflect not only Sn–O(2) but also Sn–O_i. The calculated distances for Sn–O_i and W–O_i strongly depend on the position of O_i formation (Fig. S6, ESI†). Among the calculated structures shown in Fig. 4, structures A, B, and D can well explain the experimental findings from the XRD and EXAFS measurements. Of these, the most stable energy was calculated for structure D. However, the energy differences between the structures were within 40 meV per atom; thus, structures A, B, and D might coexist in actual samples.

In general, interstitial oxygen defects in oxides generate hole carriers. However, first-principles calculations suggest that the O_i in SnO does not contribute to hole/electron conductivity because there is no defect transition level in the calculated band gap.[36,37] Furthermore, the lone-pair electrons around the NN Sn ions are absorbed by O_i, and consequently, the density of states around the VBM is drastically decreased.[36] This phenomenon potentially triggers a decrease in the hole carrier density.

Conclusions

In summary, the dependence of hole carrier density on O_2 gas concentration during the annealing of α-$SnWO_4$ was investigated. The objective was to be able to tune these carrier densities *via* adjustments to the O_2 gas concentration. It was observed that the hole carrier density increased by two orders of magnitude and achieved a value close to 10^{19} cm^{-3} at an optimum O_2 gas concentration. At O_2 gas concentrations higher than the optimum, the hole carrier density decreased and became finally saturated at approximately mid-10^{17} cm^{-3}. Both experimental and theoretical approaches showed that the first increment in the hole carrier density was well explained by the suppression of oxygen vacancy formation, whereas the subsequent decrease in hole carrier density could be due to the formation of interstitial oxygen. This study confirms the necessity of fine-tuning thermodynamic conditions to improve the semiconducting properties of Sn^{2+}-based p-type oxides.

Author contributions

M. M., N. K., and K. N. designed the experiments. Y. D. synthesized the materials. M. M., Y. D., N. K., A. S., and Y. A. performed the EXAFS measurements. M. M., N. K., A. S., and T. H. performed the SR-XRD measurements. X. H., Ta. K., and To. K. simulated the structural deformation based on density functional theory calculations.

Conflicts of interest

There are no conflicts of interest to declare.

Acknowledgements

We thank Dr H. Nitani and Dr H. Sagayama for providing technical support for the beamline experiments. M. M. would like to thank Dr H. Ohta for checking the reproducibility of the thermopower measurements. This work was supported by Grant-in-Aid for Scientific Research (No. 18K04946 and

18K05285) from the Japan Society for the Promotion of Science (JSPS). The work at KEK-PF was performed with the approval of the Program Advisory Committee (Proposals No. 2019G543, 2020G542, and 2021PF-Q009) at the Institute of Materials Structure Science, KEK. We would like to thank Editage (**www.editage.com**) for the English language editing.

Notes and references

1 J. Shi, J. Zhang, L. Yang, M. Qu, D.-C. Qi and K. H. L. Zhang, *Adv. Mater.*, 2021, **33**, 2006230.
2 H. Kawazoe, M. Yasukawa, H. Hyodo, M. Kurita, H. Yanagi and H. Hosono, *Nature*, 1997, **389**, 939.
3 Z. Wang, P. K. Nayak, J. A. Caraveo-Francas and H. N. Alshareef, *Adv. Mater.*, 2016, **28**, 3831.
4 H. Kawazoe, H. Yanagi, K. Ueda and H. Hosono, *MRS Bull.*, 2000, **25**, 28.
5 G. Hautier, A. Miglio, G. Ceder, G.-M. Rignanese and H. Gonze, *Nat. Commun.*, 2013, **4**, 2292.
6 H. Hosono, *Thin Solid Films*, 2007, **515**, 6000.
7 Y. Ogo, H. Hiramatsu, K. Nomura, H. Yanagi, T. Kamiya, M. Hirano and H. Hosono, *Appl. Phys. Lett.*, 2008, **93**, 032113.
8 T. Li, S. Luo, X. Wang and L. Zhang, *Adv. Mater.*, 2021, **33**, 3008574.
9 J. A. Caraveo-Frescas, P. K. Nayak, H. A. Al-Jawhari, D. B. Granato, U. Schwingenschlögl and H. N. Alshareef, *ACS Nano*, 2013, **7**, 5160.
10 M. Minohara, N. Kikuchi, Y. Yoshida, H. Kumigashira and Y. Aiura, *J. Mater. Chem. C*, 2019, **7**, 6332.
11 M. Minohara, A. Samizo, N. Kikuchi, K. K. Bando, Y. Yoshida and Y. Aiura, *J. Phys. Chem. C*, 2000, **124**, 1755.
12 A. Bhatia, G. Hautier, T. Nilgianskul, A. Miglio, J. Sun, H. J. Kim, K. H. Kim, S. Chen, G.-M. Rignanese and X. Gonze, *Chem. Mater.*, 2016, **28**, 30.
13 N. Kikuchi, A. Samizo, S. Ikeda, Y. Aiura, K. Mibu and K. Nishio, *Phys. Rev. Mater.*, 2017, **1**, 021601.
14 A. Samizo, N. Kikuchi, Y. Aiura, K. Nishio and K. Mibu, *Chem. Mater.*, 2018, **30**, 8221.
15 M. Minohara, Y. Dobashi, N. Kikuchi, A. Samizo, K. Tsukuda, K. Nishio, K. Mibu, H. Kumigashira, I. Hase, Y. Yoshida and Y. Aiura, *Inorg. Chem.*, 2021, **60**, 8035.
16 J. Shi, E. A. Rubinstein, W. Li, J. Zhang, Y. Yang, T.-L. Lee, C. Qin, P. Yan, J. L. MacManus-Driscoll, D. O. Scanlon and K. H. L. Zhang, *Adv. Sci.*, 2022, **9**, 2104141.
17 M. Minohara, N. Kikuchi, K. Tsukuda, Y. Dobashi, A. Samizo, K. Nishio, X. He, T. Katase, T. Kamiya and Y. Aiura, *Mater. Des.*, 2022, **216**, 110549.
18 Y. Hu, X. Yao, D. G. Schlom, S. Datta and K. Cho, *Chem. Mater.*, 2021, **33**, 212.
19 S. Katayama, Y. Ogawa, H. Hayashi, F. Oba and I. Tanaka, *J. Cryst. Growth*, 2015, **416**, 126.
20 S. Katayama, H. Hayashi, Y. Kumagai, F. Oba and I. Tanaka, *J. Phys. Chem. C*, 2016, **120**, 9604.
21 H. Ito, T. C. Fujita and M. Kawasaki, *APL Mater.*, 2021, **9**, 101116.
22 M. Barone, M. Foody, Y. Hu, J. Sun, B. Frye, S. S. Perera, B. Subedi, H. Paik, J. Hollin, M. Jeong, K. Lee, C. H. Winter, N. J. Podraza, K. Cho, A. Hock and D. G. Schlom, *J. Phys. Chem. C*, 2022, **126**, 3764.
23 D. Dahliah, G.-M. Rignanese and G. Hautier, *J. Mater. Chem. C*, 2020, **8**, 9352.
24 A. Samizo, M. Minohara, N. Kikuchi, K. K. Bando, Y. Aiura and K. Nishio, *J. Phys. Chem. C*, 2021, **125**, 17117.
25 R. Oishi, M. Yonemua, Y. Nishimaki, S. Torii, A. Hoshikawa, T. Ishigaki, T. Morhisima, K. Mori and T. Kamiyama, *Nucl. Instrum. Methods Phys. Res., Sect. A*, 2009, **A600**, 94.
26 R. Oishi-Tomiyasu, M. Yonemura, T. Morishima, A. Hoshikawa, S. Torii, T. Ishigaki and T. Kamiyama, *J. Appl. Crystallogr.*, 2012, **45**, 299.
27 K. Momma and F. Izumi, *J. Appl. Crystallogr.*, 2011, **44**, 1272.
28 M. Nomura, T. Koike, M. Sato, A. Koyama, Y. Inada and K. Asakura, *AIP Conf. Proc.*, 2007, **882**, 896.
29 B. Ravel and M. Newville, *J. Synchrotron Radiat.*, 2005, **12**, 537.
30 G. Kresse and D. Joubert, *Phys. Rev. B: Condens. Matter Mater. Phys.*, 1999, **59**, 1758.
31 G. Kresse and J. Furthmüller, *Phys. Rev. B: Condens. Matter Mater. Phys.*, 1996, **54**, 11169.
32 J. P. Perdew, A. Ruzsinszky, G. I. Csonka, O. A. Vydrov, G. E. Scuseria, L. A. Constantin, X. Zhou and K. Burke, *Phys. Rev. Lett.*, 2008, **100**, 136406.
33 W. J. Kim, W. Chang, S. B. Qadri, J. M. Pond, S. W. Kirchoefer, D. B. Chrisey and J. S. Horwitz, *Appl. Phys. Lett.*, 2000, **76**, 1185.
34 T. Ohnishi, K. Shibuya, T. Yamamoto and M. Lippmaa, *J. Appl. Phys.*, 2008, **103**, 103703.
35 J. D. Jorgensen, B. Dabrowski, S. Pei, D. R. Richards and D. G. Hinks, *Phys. Rev. B: Condens. Matter Mater. Phys.*, 1989, **40**, 2187.
36 A. Togo, F. Oba, I. Tanaka and K. Tatsumi, *Phys. Rev. B: Condens. Matter Mater. Phys.*, 2006, **74**, 195128.
37 J. P. Allen, D. O. Scanlon, L. F. J. Piper and G. W. Watson, *J. Mater. Chem. C*, 2013, **1**, 8194.